The dust mass distribution of comet 81P/Wild 2

Journal Item

The dust mass distribution of Comet 81P/Wild 2

S. F. Green,[1] J. A. M. McDonnell,[1] N. McBride,[1]

M. T. S. H. Colwell,[1] A. J. Tuzzolino,[2] T. E. Economou,[2]

P. Tsou,[3] B. C. Clark,[4] D. E. Brownlee[5]

[1]Planetary and Space Sciences Research Institute, The Open University, Walton Hall, Milton Keynes, MK7 6AA, UK.

[2]Laboratory for Astrophysics and Space Research, Enrico Fermi Institute, University of Chicago, 933 East 56th St, Chicago Ill 60637, USA.

[3]Jet Propulsion Laboratory, California Institute of Technology, 4800 Oak Grove Drive, Pasadena CA 91109, USA.

[4]Lockheed Martin Space Systems, P.O. Box 179, MS-B0560, Denver, CO 80201, USA

[5]Astronomy Department, University of Washington, bx 351580, Seattle, WA 98195, USA.

Submitted to Journal of Geophysical Research

June 2004.

ABSTRACT

The Dust Flux Monitor Instrument (DFMI) made direct measurements of the dust environment in the mass range $10^{-14}<m<10^{-5}$ kg at comet 81P/Wild 2 during the Stardust flyby on 2 January 2004. We describe the techniques for derivation of the particle mass distribution, including updated calibration for the acoustic subsystem. The dust coma is characterised by 'swarms' and 'bursts' of particles with large variations of flux on small spatial scales, which may be explained by jets and fragmentation. The mass of the dust coma is dominated by larger particles, as was found for comets 1P/Halley and 26P/Grigg-Skjellerup. However, almost 80% of the particles were detected many minutes after closest approach at a distance of ~4000 km, where small grains dominated the detected mass flux. The mass distribution varies on small spatial scales with location in the coma, consistent with the jets and fragmentation inferred from the highly heterogeneous dust spatial distribution. The cumulative mass distribution index α (where the number of particles of mass m or larger, $N(m)\propto m^{-\alpha}$) in the coma ranges from 0.3 to 1.1. It is possible that jets and fragmentation occur in all comets but have not previously been well observed due to the limitations of detectors and flyby geometry. We estimate that 2800±500 particles of diameter 15 μm or larger impacted the aerogel collectors, the largest being ~6×10^{-7} kg (diameter ~1 mm) which dominates the total collected mass. Of these only 500±200, representing just 3% of the collected mass, originated in the far post-encounter region.

INDEX TERMS: 6015 Planetology: Comets and Small Bodies: Dust; 6210 Planetology: Solar System Bodies: Comets; 6094 Planetology: Comets and Small Bodies: Instruments and techniques; 2129 Interplanetary Physics: Interplanetary dust

KEYWORDS: cometary dust; Stardust, 81P/Wild 2; Dust Flux; DFMI

1. Introduction

Cometary dust particles, trapped in the volatile ices of the nucleus since their formation, contain information on the conditions in the pre-solar nebula, its precursor interstellar cloud and nucleosynthetic processes in the stars from which their constituent grains originally formed. The primary objective of Stardust is to capture these samples intact and return them to the Earth for in-depth microanalysis [*Brownlee et al.,* 2003]. These dust grains are the source of a major component of interplanetary dust and large (sub-mm and larger) grains are observed in cometary dust trails forming relatively long lasting meteoroid streams, which gradually dissipate into the zodiacal dust complex. Micron sized (and somewhat smaller) grains can be swept out of the inner solar system by solar radiation pressure. The contribution of comets to the total interplanetary dust complex, and the subsequent dynamics of the individual grains, are critically dependent on the dust mass (or size) distribution. Furthermore, the dust-to-gas ratio in cometary nuclei provides constraints on the conditions in the region in which it formed.

Observations from Earth of the scattered light from cometary comae do not constrain the total emitted dust mass. Dust tail models can be used to infer crude time-averaged size distributions and mass loss rates but are still dependent on assumed model parameters. In situ measurements provide the only direct means of accurately determining the instantaneous particle mass distribution at a point within the coma. If the cumulative particle mass distribution is described by a power law, $N(m) = k\, m^{-\alpha}$ (where $N(m)$ is the number of particles larger than or equal to mass m, and k is a constant) then for a cumulative mass distribution index of $\alpha < 1$, the

total dust mass is dominated by the larger grains, and if $\alpha < 0.67$, the larger grains also dominate the total cross sectional area. However, the observed scattered light depends on the scattering efficiency as well as the cross section and small grains (of size ~ wavelength of scattered light) may contribute proportionately more due to their greater scattering efficiency. Although in-situ measurements from flyby spacecraft allow direct determination of the mass distribution along a single path through a cometary coma, the derivation of the mass distribution at the nucleus requires knowledge of the grain velocity distribution and emission process.

Direct detection, by Giotto's Dust Impact Detection System (DIDSY) [*McDonnell*, 1987; *McDonnell et al.,* 1986] and Particle Impact Analyser (PIA) [*Kissel*, 1986] at Comet 1P/Halley, of particles of mass 10^{-18} kg to 10^{-5} kg indicated a coma mass dominated by large particles and a dust to gas ratio of between 1.3 and 3 [*McDonnell et al.,* 1987, 1991]. Although the unusual nature of the four component mass distribution in Comet Halley (see Figure 9) could possibly be explained by the size dependent sampling of particles with different ejection times, corresponding to different levels of nucleus emission activity [*Perry et al., 1988*], Fulle *et al.* [2000] showed that this complex coma mass distribution is consistent with a single slope mass distribution ejected from the inner coma. However, the required source mass distribution index was shallow and therefore dominated by large particles. Large grains were also found to dominate in the second Giotto target, 26P/Grigg-Skjellerup [*McDonnell et al.,* 1993].

The objectives of the Stardust Dust Flux Monitor Instrument (DFMI) were to:

1) Measure the interplanetary dust flux,
2) Determine particle fluxes during the 81P/Wild 2 flyby,
3) Determine the particle mass distribution in the coma of 81P/Wild 2,
4) To provide the context for the collected dust samples,

5) To monitor the dust environment at P/Wild 2 for spacecraft health and interpretation of anomalies.

The DFMI combines two different dust detection techniques. The PVDF (polyvinylidene fluoride) dust sensor unit (SU) consists of a thin film of permanently polarized material. An impacting dust particle produces rapid local destruction of dipoles, resulting in a short current pulse with maximum amplitude depending on the volume of material destroyed (which depends on the impacting particle mass and speed). Two PVDF sensors are located on the main shield of Stardust. The dual acoustic sensor system (DASS), utilizes two piezoelectric crystals mounted on the first two layers of the spacecraft Whipple dust shield to measure the flux of larger particles. Figure 1 illustrates the location of the sensors and the parts of the spacecraft exposed to dust impacts during the encounter.

The Stardust encounter with 81P/Wild 2, the performance of the spacecraft and the conditions leading up to and during the encounter are described by *Tsou et al.* [2004]. The first DFMI results, which indicate a highly heterogeneous dust coma, characterised by jets and particle fragmentation, are presented by *Tuzzolino et al.* [2004] and are reviewed in Section 4. In this paper we present the derivation of the particle mass distribution at 81P/Wild 2 and investigate how the observed mass distribution can be reconciled with the explanations of the complex dust coma structure and the mass distributions observed in other comets.

2. Instrument operation and data reduction procedures

2.1 DFMI data format

The PVDF subsystem consists of two separate sensors with different sensing areas and sensitivity. The large PVDF sensor, with a 28μm film, has a sensitive area of 0.02 m^2 . The small PVDF has a sensitive area of 0.002 m^2 but with a 6 μm thick film which is more sensitive to smaller particles. Each of the two PVDF detector systems has 4 mass thresholds (m1, m2, m3, m4 for the small detector and M1, M2, M3, M4 for the large detector). The peak signal from an impacting particle is measured and the appropriate 16 bit threshold counter is incremented by one. In encounter mode the cumulative counters are read out within 0.1 s if an event is detected and every second if no impacts are detected. The cumulative counters ensure that if there is a loss of telemetry the total number of impacts is recorded correctly at each DFMI readout. The fast response of the PVDF detectors allows count rates of up to 10^4 s^{-1} to be measured with less than 5% dead time correction. If the cumulative count exceeds 65535, it overflows and continues from zero, but confusion cannot occur unless the count rate reaches unprecedented levels in excess of 10^5 per second. The PVDF sensors are described in detail by *Tuzzolino et al.* [2003].

The DASS consists of two quartz piezoelectric acoustic sensors mounted on the rear of one half of the front bumper shield within the launch adapter ring (A1) and on a circular sounding sheet attached in front of the first NEXTEL curtain immediately behind the front bumper shield (A2). The A2 sensor is directly behind the A1 sensor as shown in Figure 1.

The limited resources available for the acoustic sensors mean that the transmitted counts do not relate directly to individual impacts. An understanding of the operation of the sensors is required to interpret the results and define the uncertainties in derived fluxes. The output voltage obtained from the sensors is a complex sinusoidal (frequency ~20 kHz) oscillation within a

decaying envelope, which has an initial sharp rise to a peak voltage V_p, and a gradual quasi-exponential decay with a time constant of a few milliseconds. V_p is related to the particle impact momentum and position on the shield. Figure 2 illustrates the characteristics of the A1 sensor output for an impact on the front shield. The limitations on mass and data rate for the acoustic subsystem mean that V_p cannot be measured over a large dynamic range. Instead, the waveform is characterised by two counts,"N_1" and "N_2". If the output voltage exceeds the threshold V_1 during a fixed time interval T_1, then N_1 is incremented by 1, and similarly for N_2 (see Figure 1). Thus N_1 (or N_2) represents the number of time intervals over which the signal is (at some time during the interval) above the voltage threshold V_1 (or V_2). A large impact will produce a large V_p and a long duration signal giving a large change in N_1 and N_2, whereas a small signal will produce only a small change in N_1. The encounter data consist of N_1 and N_2 cumulative counts at the end of sample read out periods of between 0.1 and 1.0 s depending on the signals detected by the PVDF sensors. T_1 and T_2 are 510 and 210 μs respectively, giving maximum possible N_1 and N_2 values of 1960 and 4762 in 1 second read outs. However, the N_1 and N_2 counters were restricted to 8 bits (256 increments) so it was possible that multiple or large events could cause the counters to overflow. The pre-encounter predicted peak flux at closest approach was around 1 dust impact per second detectable by the acoustic sensor so multiple events and/or overflows were not expected to affect the majority of the data.

2.2 Acoustic sensor calibration

The derivation of the mass of an individual impacting particle on the acoustic sensors requires knowledge of the impact position and the detector sensitivity. Since the position is unknown, a given signal, characterised by V_p or N_1 (and possibly N_2), may be the result of a

small impact close to the sensor or a large impact further away. The derived momentum (and hence mass) of an impactor is therefore represented by a probability function rather than a specific value. This is also true for the mass thresholds corresponding to events that just trigger the sensor (i.e. N_1=1). For a given particle mass, the sensitive area of the shield is obtained from absolute momentum calibration, obtained with University of Kent Light Gas Gun (LGG) shots at a fixed distance from a sensor on a small section of flight-representative shield, combined with relative signal attenuation as a function of impact position, obtained from 'bead drops' over the whole shield.

Preliminary calibration is described by *McDonnell et al.* [2000] and *Tuzzolino et al.* [2003]. Figure 3 illustrates the updated acoustic sensor sensitivity derived from LGG tests. The sensor was attached to a 10 x 10 cm tile of shield material and powered with the same circuit as the flight sensors (conditioning of the output signal did not include the amplification that occurs in the flight electronics). The nominal impact position was defined as 4 cm from the sensor and a correction was made to the output signal to account for the different acoustic response of the shield as a function of position.

The signal from an impact at distance r from a piezo-electric transducer is related to the particle mass, m, by

$$V_p = \varepsilon(v)\, m\, v\, R\, S \qquad \textbf{(1)}$$

for non-penetrating impacts, where S is the detector sensitivity (in Volts per unit momentum) for an impact at distance r_o from the detector, R is the relative sensitivity between distance r and r_o, ε

is the momentum enhancement and v is the impact speed. The velocity-dependent momentum enhancement is the additional momentum imparted to the target by ejection of material from the impact site. We find $\varepsilon = 2.0 \pm 0.2$ at $v = 6$ km s^{-1} based on laboratory tests performed with a sensor attached to a solid metal target. However, a composite target may produce large ejecta fragments which could result in a significantly different enhancement. For particles which penetrate the shield, the enhancement factor must be derated to account for the momentum which is transferred through the target and not captured:

$$\varepsilon' = \varepsilon\,(m_{pen}/m)^{\gamma} \qquad \textbf{(2)}$$

where m_{pen} is the mass at which the target is just penetrated and γ is the momentum derating factor. A value of $\gamma = 0.4 \pm 0.1$, derived from Giotto data [*Perry,* 1990], is adopted here. The particle momentum (and hence mass) is known for the LGG impact tests which were conducted at ~6 km s^{-1}. However, the measured signal implicitly includes momentum enhancement at the same level as will be experienced in the cometary flyby and hence eliminates uncertainty in this value.

Figure 3a shows the results for all LGG shots with well determined signals and velocities. The effect of non-linearity of the sensor is clearly apparent above $V_p = 3$ V and it is totally saturated at approximately 9 V. Although it is relatively easy to produce low speed impacts of low momentum (as used for the relative shield calibration) we have confined our absolute calibration to LGG impacts at close to the true impact speed for particles at P/Wild-2 (6.12 km s^{-}

[1]), to ensure similar momentum transfer conditions. Figure 3b illustrates a least squares fit to non-penetrating glass particle data to obtain an absolute calibration.

The attenuation of the signal strength as a function of impact position was measured using bead drops on a full size mock-up of the bumpershield, with the acoustic sensor placed as on the flight model. Repeated measurements were made using a 1.5 mm diameter stainless steel bead dropped from a height of 15 cm (the non-uniform nature of the surface and variation in the momentum transfer process caused an inherent scatter of up to 50% in the individual signals). Drops were carried out over the whole shield on a grid with mesh size 1 cm near the sensor and 5 cm at large distances from the sensor. All measured signals were below 2.5V where the sensor output is essentially linear with momentum. The averaged maximum amplitudes of the resulting signals are shown in Figure 4 as a response map of the shield. The shield response as a function of distance from the sensor is not the same for the X and Y axes, (or even for the positive and negative Y axes), probably due to the non-uniform weave of the composite material comprising the top surface of the bumpershield. Since the LGG test shots were fired at a range of positions relative to the sensor on the 10 cm square shield sections, this may explain the relatively large scatter in the data in Figure 3.

We need to determine an average signal at the reference distance of 4 cm from the sensor to link the relative and absolute calibrations. Figure 4b shows signals versus distance (between 2 and 7 cm) from the sensor. There is a large scatter overall due to the asymmetric response of the shield. When a single axis is considered (data corresponding to two orthogonal axes are illustrated in Figure 4b) the sensitivity follows an exponential decay with distance from the

sensor. The overall fit shown yields a relative signal of 0.72 V at 4 cm from the sensor. The relative sensitivity, R_i, of any location, i, on the shield is therefore obtained by dividing the measured bead drop signal by 0.72 V.

2.3 Mass thresholds and flux determination

The derivation of flux (number of impacts per m^2 per second) or fluence (time integrated flux) for the PVDF sensors is straightforward. The sensors were calibrated using dust particles at 6.1 km s^{-1} in the dust accelerators at Munich and Heidelberg. The mass thresholds, defined in the instrument electronics, are shown in Table 1. A given detectors is equally sensitive over its whole area. Although the mass thresholds are well defined (±10%) from the calibration, this was performed using high density particles. The signal is proportional to the volume of depolarisation, which in turn is approximately proportional to particle size. Since the cometary grains may have densities ranging from ~3500 kg m^{-3} for silicate cores, to as low as 100 kg m^{-3} for large fluffy aggregates [*Fulle et al*., 2000], the mass of a cometary grain producing a given signal is much more uncertain. We have thus assigned uncertainties of a factor of two in mass to each threshold.

The situation is more complex for the acoustic sensor data. The absolute sensitivity of a small area on the shield (element i) is determined from the relative sensitivity *R*i and the LGG calibration at 4 cm from sensor, *S* (in fact εS is measured, see Section 2.2). Detection thresholds are set in the flight electronics at 0.1 and 1.0 V, which are equivalent to a high sensitivity channel voltage threshold V_1 = 0.005 V and a low sensitivity channel voltage threshold V_2 = 0.05 V for the unamplified sensor output.

The mass threshold (m_i) for each shield element is determined from equations (1) and (2):

$$m_i = V_p /(\varepsilon S v R_i) \quad \text{for } m_i < m_{pen} \quad \textbf{(3)}$$

$$m_i = [V_p /(\varepsilon S v R_i (m_{pen})^{\gamma})](1/(1-\gamma)) \quad \text{for } m_i > m_{pen} \quad \textbf{(4)}$$

As the velocity of the impactor is known (at P/Wild-2 where all cometary grains will impact normal to the shield at 6.12 km s^{-1}), then m_i can be determined.

In order to derive a particle flux or fluence for the acoustic data, the effective area of the detector is required. The effective area accounts for the fact that the flux of impacting particles will have some (unknown) mass distribution. The signals from all possible particle masses at all possible impact sites on the shield are calculated, assuming a cumulative mass distribution $N(m) = km^{-\alpha}$, such that a probability of a particle of a given mass being detected can be calculated. This probability function (which is a function of particle mass), when multiplied by the actual sensing area (which is also a function of mass) produces an *effective* sensing area as a function of the limiting mass. Thus the number of particles detected can be converted to a flux (or fluence) at any chosen mass limit, since the effective area for that mass limit will ensure that the flux (or fluence) is consistent with the assumed input mass distribution. As the *actual* mass distribution is unknown, the calculation of effective area is iterative. An initial value of α is assumed, and the fluences calculated, which thus defines the empirical mass distribution index, which can be fed back into a new calculation of effective area. Figure 5a illustrates the effective area of the front

shield, A_{eff}, as a function of cumulative mass index α. The threshold mass for the front shield acoustic sensor, $m(N_1)$ = 3 x 10^{-11} kg, is chosen such that approximately 90% of all detected particles have masses larger than this threshold (Figure 5b). Although there is some uncertainty in the threshold mass $m(N_1)$, (a conservative value of a factor of 3 is applied here), the ratio $m(N_2)/m(N_1) = 10$, is precisely defined by the choice of threshold voltages V_1 and V_2.

The rear shield sensor, A2, operates in the same manner as the front shield sensor, with counts denoted by N_3 and N_4 for the low and high voltage thresholds. It detects both the remnants of the incident particle and fragments of ejecta from the exit hole of the front shield. LGG shots at approximately 6 km s^{-1} show a variety of ejecta patterns and impact signals dependent on the impactor properties. The mass threshold corresponding to a detected N_3 signal (which is only marginally larger than the threshold for penetration reported by *Tuzzolino et al.* [2003]), is $(2^{-1.2}/_{+2})$ x 10^{-7} kg. The uncertainty is based on the scatter in the limited experimental data for different impactor materials. The mass threshold for N_4 is fixed at precisely 10 times that of N_3. The effective area of the rear shield sensor is currently not known since it has not been possible to conduct hypervelocity impact tests due to the large size of the shield. However, we can place constraints on the effective area, from the maximum size of the shield ($0.7m^2$) and the size of expected ejecta cones, which gives a minimum area ~0.1 m^2. We thus adopt an effective area of $(0.3^{-0.2}/_{+0.4})$ m^2 for the encounter data.

3. Instrument performance

The DFMI was activated shortly after launch to monitor interplanetary dust particles. However, the instrument became noisy during cruise operation due to an unidentified cause. The noise eventually affected all counters and in the most sensitive counter (m1) it saturated within a few seconds. During subsequent tests it operated nominally for between 35 and 40 minutes before a well-defined onset of noise, when the power consumption increased drastically and multiple error event reports (EVRs) were generated by the spacecraft. Thus the effects of the noise could be avoided by operating for no more than 30 minutes at a time, and so the decision was taken to operate DFMI for only 30 minutes centered on the predicted time of closest approach to 81P/Wild 2, with updated software ensuring that the instrument would switch off if EVRs occurred. The instrument performed nominally at the encounter test (Annefrank asteroid encounter on 2 November, 2002) and throughout the 81P/Wild 2 encounter itself.

The first dust impact detected by DFMI was with the acoustic sensor A1 at –264 s at a cometocentric distance of r = 1630 km (all times are referred to closest approach at UT 19:21:32 on 2 January 2004, with a closest approach distance of r = 236.4 ± 1 km [*Tsou et al.,* 2004]). The event rate gradually increased up to closest approach and then decayed afterwards with a second period of high activity between +620 s (r = 3810 km) and +720 s (r = 4420 km). The last detected particle was at +922 s at a cometocentric distance of r = 5650 km.

The PVDF sensor counters recorded 8683 impacts in total, with the majority in the most sensitive channel, m1. There were therefore no overflows of the counters and the maximum count rates did not exceed 10^4 per second.

In order to determine the impact rates for the acoustic sensors, the time intervals where counts were detected must be considered individually. In total, 106 time intervals contained non-zero N_1 counts, 42 contained non-zero N_2 counts, 10 contained non-zero N_3 counts and 1 contained non-zero N_4 counts. In all cases where N_3 was non-zero there was a signal in N_1 and N_2 in the same or a preceding time step, indicating that the penetrations detected by the rear shield A2 sensor were also detected by the A1 sensor. The actual number of impacts that produced these events have been derived by considering the N_2/N_1 ratios, coincidence of N_3 with N_1, and statistical considerations to derive impact numbers. Although it was possible for multiple or large events to cause the 8 bit acoustic sensor counters to overflow more than once during one time interval (i.e. counts exceeding 255), there is no evidence for this occurring even during the highest activity periods. The largest individual counts were N_1=142, N_2=126, N_3=58 and N_4=29. (The N_1 counters overflowed 10 times during the course of the encounter and the N_2 counter 3 times). The data are best explained by 107+n impacts, where n is some undetermined number of small particles with very low signals, close to the detection threshold and thus 'hidden' among the signals from the larger unambiguously detected particles. Using the local event rate to predict the probability of a given number of particles in each time step results in a prediction of 133 impacts (i.e. 107 + n = 133) triggering the lowest threshold (channel 1). The number of particles triggering N_2 counts (channel 2) is 41, while 7 particles penetrated the front shield (channel 3), three of which resulted in signals which straddled two sample periods. For the determination of the encounter fluence we therefore adopt 133±30 impacts in channel 1 (AC1), 41±7 impacts in channel 2 (AC2), 7±3 impacts in channel 3 (AC3) and 1±1 impact in channel 4 (AC4). The assigned uncertainties are based on √n statistical uncertainties for channels 2 to 4 and the expected range of events for channel 1.

4. Spatial distribution of dust at 81P/Wild 2

Figure 6 illustrates the count rates in the most sensitive PVDF channel (m1) and acoustic sensor channel (AC1) as a function of time (i.e. position along the trajectory). The PVDF data (which are plotted on a logarithmic scale), show extreme variations in flux which occur on timescales of 0.1 seconds or less [*Tuzzolino et al.,* 2004]. They indicate a highly heterogeneous coma characterised by 'swarms' (10 – 100 km scales) and 'bursts' (≤ 1 km scales) respectively. This structure is interpreted as due to a combination of jets and fragmentation and is discussed in detail by *Tuzzolino et al.* [2004], *Sekanina et al.* [2004] and *Clark et al.* [2004]. We discuss only the main features here.

The swarms observed by Stardust have spatial scales similar to the narrow jets present in the Stardust camera images [Brownlee *et al.* 2004]. 'Jets' have traditionally been attributed to the emission of dust from discrete 'active regions' on the nucleus with dust traveling approximately radially away from the local surface normal. However, 3D fluidodynamical coma models are characterized by shocks resulting from non-radial gas flow that depend critically on the nucleus shape and topography (but do not require discrete active regions). This implies that the dust particles in the inner coma are also concentrated along the gas flow discontinuities creating the visual impression of jets [Crifo *et al.* 2002] even though the dust may originate from different areas on the nucleus surface. However, there are a number of fundamental problems with this interpretation of the spatial distribution of dust detected by Stardust. The spacecraft was always well outside the inner coma region, i.e. outside the region where the dust dynamics is dominated by forces due to gas drag. Thus, whatever the mechanism for the observed structures in the

Stardust data, if they originate in the inner coma the grains must travel in near-radial or near-parallel paths to maintain the narrow structures observed, or be produced locally. The fluidodynamic models produce local spatial density enhancements generally much less than a factor of 2 for the gas. Small (sub-micron) dust grains will be entrained in the gas flow but larger grains will be progressively less affected. The density enhancements for Stardust swarms are significantly greater than this (e.g. the average spatial density in the swarm between +2 s to +4 s is 50 m^{-3} in PVDF sensor channel 1 (grains of diameter ~3 μm) compared with <0.04 m^{-3} in the preceding 2 seconds). Stardust provided the first very high resolution (<1 km) information on how the dust spatial density varies as you pass through some of these 'jet' features. It is the extremely large flux variations on such small scales in the Stardust 'bursts' that leads to the conclusion that fragmentation must be responsible. This conclusion is driven by the fact that neither the active-region-and-jet model nor the fluidodynamic model, can explain counts near closest approach that remain at zero for 15 seconds (spatial density $<5x10^{-3}$ m^{-3}) then jump to five hundred counts within 0.1 seconds (spatial density of 400 m^{-3}). A mechanism which produces local enhancements in spatial density must be responsible.

If we accept that fragmentation is the mechanism for the observed enhancements, then it is clear that either the process occurs with low energy (i.e. the daughter particles have small relative velocity dispersion) in order for the fragmentation cloud to remain coherent on the observed scales, or that it occurs very close to the spacecraft. If the fragmentation process was accompanied by volatile emission, resulting in a large velocity dispersion, the fragmentation cloud would dissipate rapidly. A quantitative model of fragmentation is required to investigate in detail how the features observed by Stardust arise, how the fragmentation process might be constrained and how it affects the overall coma properties.

The second period of activity, between +620 and +720 s which accounted for over 80% of the total number of particles detected, lies at approximately the location predicted for the terminal shock [e.g. Crifo *et al.* 2000]. However, the structure and spatial density enhancements observed are also incompatible with passage of Stardust through a single jet or a terminator shock. At this large cometocentric distance, remarkable collimation of trajectories would be required to maintain the observed structures. The entire period of activity subtends an angular size at the near nucleus region of ~0.5º and contains structure with large changes of flux with angular size of <0.01º. The mean spatial density within the region is 2 m^{-3} but is less than 10^{-3} m^{-3} in the 100 second periods preceding and following its passage. Spatial density variations of up to 100 within 1 km are found within this region. The feature is explained by *Sekanina et al.* [2004] as activity from, or fragmentation of a large (meter sized) particle ejected at a previous apparition.

5. Dust mass distribution at 81P/Wild 2

The cumulative fluence for the whole encounter is illustrated in Figure 7. The PVDF small and large sensors and the acoustic A1 sensors represent independent datasets, but are consistent with a single slope mass distribution in the coma with $\alpha = 0.85 \pm 0.05$ for masses below 10^{-9} kg. However, it is clear that the mass distribution varies significantly throughout the encounter. In order to compare the fluence with other comets, we have excluded the post-encounter swarms of particles beyond +600 s (Figure 8a). The data are well fitted by a single slope mass distribution with $\alpha = 0.75 \pm 0.05$. The mass distributions for the comae of comets Halley and Grigg-Skjellerup are shown for comparison in Figure 8b. The three mass distributions

are reasonably similar in shape although, noting the logarithmic scales, small differences in slope may be significant. As was found for 1P/Halley [*McDonnell. et al.,* 1987], the mass index below 10^{-9} kg implies a coma dominated by scattered light from small particles at 81P/Wild 2. However, the large grain excess (for masses above 10^{-9} kg) seen at Halley and also apparently present at Wild-2 contribute almost half the total particle cross-section in the sampled coma. In both cases the total mass in the coma is dominated by the large particles. The form of the large particle excess in the coma at masses above 10^{-9} kg may be better determined when individual particle masses are derived for the larger impacts detected by the acoustic sensors.

Two questions arise from these results:

1) If fragmentation and jets play such a key role in the detected coma mass distribution, why does the overall mass distribution bear such a close resemblance to previously observed comets?
2) Why are there no small particles (as measured by the PVDF detectors) coincident with the larger particles detected by the acoustic sensors before $t = -50$ s and between $t = -12$ and +1 s (see Figure 6)? This might be particularly surprising when one considers that fragmentation is apparently so important.

Firstly, the structure seen at 81P/Wild 2 may be present in *all* cometary comae. Images taken during the close flybys of comets 1P/Halley [*Thomas and Keller,* 1987] and 19P/Borrelly [*Soderblom et al.,* 2004] revealed filamentary jets in the inner coma of spatial scales similar to those seen by the Stardust camera [*Brownlee et al.,* 2004; *Newburn et al.,* 2004] and detected as 'swarms' by DFMI. In addition, detection of optical scattering by grains at 26P/Grigg-Skjellerup

also showed high concentrations of particles interpreted as jets [*McBride et al*., 1997]. All these observations are however, of light scattering by dust grains along a line of sight. No previous detections of structure on the km scale have been made directly by in-situ dust detectors due to the higher fly-by speeds (1P/Halley), lack of suitable detectors (19P/Borrelly) or reduced sensitivity (26P/Grigg-Skjellerup). However, 'clusters' and 'packets' of particles with similar characteristics were identified at distances of order 10^5 km from the nucleus of comet 1P/Halley by the DUCMA instruments on the Vega 1 and Vega 2 spacecraft [*Simpson et al.,* 1987]. In addition, none of these in-situ data are inconsistent with the structures observed at 81P/Wild 2. Figure 9 illustrates the Stardust data rebinned to the same resolution as the Giotto DIDSY data at 1P/Halley and it is seen that the fine detail is completely lost. The three observed overall mass distributions (Figure 8b) may simply be the natural consequence of flybys through structured comae all undergoing the same physical processes in all three cases. These physical processes certainly include those that produce visible jets in all three cases and fragmentation at least for Wild 2.

Secondly, all housekeeping data for the instrument was nominal and the cumulative counters indicate that there are no periods of missing data. In fact, if the 'gaps' between the high count rates detected by the PVDF sensor were due to data drop-outs, the total coma brightness (and the implied total dust production rate) would exceed that observed from ground-based telescopes in scattered light and thermal emission, by two orders of magnitude! The lack of a detection in a given channel does not necessarily mean that no particles are present, merely that the probability of detection is low. The sensitive area of the PVDF detectors is significantly smaller than that of the acoustic sensors so the detection of 1 impact (or the upper limit if no

detection is obtained) results in a much higher derived flux value. Statistically there is equal probability of a detection in the PVDF sensor channel m1 as with the acoustic sensor channel AC1 when the cumulative mass index $\alpha = 0.5$. Although, on average, the overall mass index in the inner coma is steeper than this value, it is the result of a combination of jets (plus 'background' coma) with very different mass distributions. The terminal velocities of dust particles when they leave the near nucleus region (i.e. within a few tens of nucleus radii where gas drag provides the dominant force), are dependent on the particle size, shape and density. The resultant velocity dispersion, combined with the rotation of the nucleus will typically result in detection of a narrow range of particle masses by a spacecraft instantaneously crossing a jet. Such structures were inferred at comet 1P/Halley [*Mazets et al.,* 1987; *Vaisberg et al.,* 1987; *Simpson et al.* 1987]. It is therefore possible for there to be detection of larger grains by the acoustic sensors with few or no particles at smaller sizes detected by the PVDF sensors (or vice versa). Both examples are seen in the encounter data at $t = -12$ s to +2 s and $t = +2$ s to +4 s respectively (see Figure 6). Velocity dispersion will also be present if grain fragmentation occurs inside the inner coma. However, if it occurs beyond the point where gas drag is significant then both the parent and daughter particles will have the same velocities until differential radiation pressure forces cause dispersion. Figure 10 shows the mass distributions for selected time periods to illustrate where this effect may be visible. Figure 10a covers the period between –33 s and –25 s where fragmentation appears to have occurred outside the near nucleus region. The best fit mass distribution is $\alpha = 0.75$ for $m < 10^{-9}$ kg. Note that one shield-penetrating particle is detected in this period and the upper limits at all masses do not rule out a lower slope in the mass distribution for $m > 10^{-9}$ kg. The same value of the mass distribution index, ($\alpha = 0.75$), is obtained for the period between +2 s and +4 s (shown in Figure 10b), but only for particles

smaller than $m = 10^{-11}$ kg. Also, in this case, the upper limits at larger masses preclude a flattening of the mass distribution and in fact imply a steep cut-off for masses above 10^{-11} kg. This period is characterised by a <0.2 s 'burst' with over 1100 particles detected on the small PVDF sensor. This may be explained by one of two processes: either the detection of a jet where fragmentation has occurred predominantly within the near nucleus region and any larger grains have not reached the spacecraft location, or by almost complete fragmentation of the larger grains such that their spatial density is below the detection threshold. Figure 10c shows all the data up to –33 s where only 3 small particles were detected by the PVDF sensors. This is consistent with the very shallow mass distribution index $\alpha = 0.33$ for $m < 10^{-9}$ kg (and which may hold up to $m \sim 10^{-9}$ kg). In the period between –12 s and +1 s (Figure 10d) there appear to be several 'swarms' with no small particles detected. These may be jets where the spacecraft has intercepted only the larger grains (the smaller ones having been accelerated past its position). The dashed line indicates that a very shallow mass distribution index of $\alpha = 0.3$ is consistent with these data.

The coma of 81P/Wild 2 is characterised by localised regions with a wide range of mass distributions which can be understood by the passage of Stardust through jets and particle fragmentation clouds. The overall mass distribution, which is similar to that seen at 1P/Halley, is a result of the combination of these different mass distributions.

The mass distribution for the period after +600 s is shown in Figure 11. No shield penetrations were detected, consistent with the very high mass index $\alpha = 1.13 \pm 0.2$ and the interpretation of the feature as due to emission from a local source.

The mass distributions measured by DFMI can be used to estimate the number of particles in the aerogel collectors. The primary objective of Stardust was to collect at least 1000 particles of diameter 15 μm or larger. Although much lower densities may be possible for the larger grains, we adopt a conservative particle density of 500 kg m^{-3}. If the density is lower, then the numbers of collected particles will be larger than the numbers calculated here. The collecting area of the aerogel sample tray is 0.1039 m^2 [*Tsou et al.,* 2003]. From the data in Figure 8, we estimate that 2300±400 particles were collected in the inner coma. Although almost 80% of the particles detected by DFMI were in the post-encounter period between +620 s and + 720 s, they were almost entirely detected in the lowest mass channel. We estimate, from the data shown in Figure 11, that 500±200 particles of 15μm or larger will be have impacted the aerogel during this period.

The mass distributions can also be used to estimate the total mass of cometary dust collected. Because of the small cumulative mass index in the coma, the total mass is dominated by the largest particle. We estimate that the largest single particle impacting the spacecraft is ~ 2 x 10^{-5} kg (i.e. ≈ 4 mm diameter). This is consistent with the non-triggering of the thrusters to compensate for any large off-axis impact on the spacecraft ($m > \sim 10^{-4}$ kg). The estimated largest single mass impacting the aerogel is ~ 6 x 10^{-7} kg (≈ 1.3 mm diameter) which dominates the total collected mass (although a particle of this size could possibly punch through a cell of aerogel altogether and therefore may not be recovered). The high cumulative mass index in the post – encounter high activity period means that only ~3% of the collected mass will have been collected in this region.

The sample collector, when returned to Earth in 2006, will provide both an independent confirmation of the total mass distribution and an indication of the effect of the capture process on the size distribution of the residual particles trapped in the aerogel. This is because a significant fraction of the cross-section of the collector is made up of the aerogel cell support frame which is covered with aluminum foil. This foil will provide a cratering record of the impactors in a material which has been extensively calibrated in the laboratory and used in Earth-orbiting experiments. The size distribution derived from the crater size distribution can then be compared both with the particles captured in the aerogel (and the entry hole cross-sections) and the in-situ data. Since the cratering is a size dependent process and the DFMI data are sensitive to mass, some additional insight may be gained into the original (i.e. pre-capture) densities of the particles.

Acknowledgements

We are indebted to the Stardust project for the invitation to include the acoustic sensors on the Stardust payload. The Open University acknowledge the financial support of the UK Particle Physics and Astronomy Research Council. M.J. Burchell, B.A.M. Vaughan, A.P.T Allen and F.I. Allen of the University of Kent performed many of the calibration measurements.

References

Brownlee, D. E., *et al.* (2003), Stardust: Comet and interstellar dust sample return mission, *J. Geophys. Res.* **108**(E10), SRD -1 1-12.

Brownlee, D.E. et al. (2004), Surface of Young Jupiter Family Comet 81P/Wild 2: View from the Stardust Spacecraft, *Science*, **304**, 1764-1769.

Clark, B. C., S. F. Green, T. E. Economou, S. A. Sandford, M. E. Zolensky and D. E. Brownlee (2004), Release and fragmentation of aggregates to produce lumpy coma streams, *J. Geophys. Res.,* submitted.

Crifo, J. –F. and A.V. Rodionov (2000), The dependence of the circumnuclear coma structure on the properties of the nucleus, *Icarus*, **148**, 464-478.

Crifo, J. –F., A.V. Rodionov, K. Szego and M. Fulle (2002), Challenging a paradigm: Do we need active and inactive areas to account for near-nuclear jet activity? *Earth Moon & Planets* **90**, 227-238.

Fulle, M., A.C. Levasseur-Regourd, N. McBride & E. Hadamcik (2000). In situ measurements from within the coma of 1P/Halley: First order approximation with a dust dynamical model, *Astron. J.,* **119**, 1968-1977.

Kissel, J. (1986), The Giotto particulate impact analyser, in *The Giotto Mission – its Scientific Investigations*, ESA SP-1077, 67-83.

Mazets, E. P., *et al.* (1987), Dust in comet P/Halley from Vega observations, *Astron. Astrophys.* **187**, 699-706.

McBride, N., S. F. Green, A. -C. Levasseur-Regourd, B. Goidet-Devel and J. B. Renard, J.-B. (1997), The inner dust coma of comet 26P/Grigg-Skjellerup: multiple jets and nucleus fragments? *Mon. Not. R. Astron. Soc.* **289**, 535-553.

McDonnell, J. A. M. (1987), The Giotto Dust Impact Detection System, *J. Phys. E.,* **20**, 741-758.

McDonnell, J.A.M., *et al.* (1986), The Giotto Dust Impact Detection System, in *The Giotto Mission - Its Scientific Investigations,* ESA SP-1077, 85-107.

McDonnell, J. A. M. *et al*. (1987), The dust distribution within the inner coma of comet P/Halley 1982i: Encounter by Giotto's impact detectors, *Astron. Astrophys.,* **187**, 719-741.

McDonnell, J.A.M., P. L. Lamy and G. S. Pankiewicz (1991), Physical properties of cometary dust, in *Comets in the Post-Halley Era Volume 2,* (R. L. Newburn, M. Neugebauer, J. Rahe, Eds.) Kluwer, Dordrecht, 1043-1073.

McDonnell, J. A. M. *et al.* (1993), Dust particle impacts during the Giotto encounter with comet Grigg-Skjellerup, *Nature*, **362** 732-734.

McDonnell, J.A.M *et al.* (2000), The Stardust Dust Flux Monitor, *Adv. Space Res.,* **25**, 335-338.

Newburn, R.L., T. C. Duxbury and D.E. Brownlee, (2004), STARDUST imaging experiment at comet 81P/Wild 2, *J. Geophys. Res.*, this issue.

Perry, C. H. (1990), In-situ Dust Mass Distribution measurements from the Giotto Encounter with Comet P/Halley, Ph.D. Thesis, University of Kent at Canterbury, Canterbury, UK.

Perry, C. H., S. F. Green and J. A. M. McDonnell (1988), A possible explanation for the inconsistency between the Giotto grain mass distribution and ground-based observations, in *Infrared Observations of Comets Halley & Wilson and Properties of the Grains,* NASA Conf. Publ. 3004, 178-180.

Sekanina, Z., D. E. Brownlee, T. E. Economou, A.J. Tuzzolino and S. F. Green (2004), Modeling the Nucleus and Jets of Comet 81P/Wild 2 Based on the Stardust Encounter Data, *Science*, **304**, 1769-1774.

Simpson, J. A., D. Rabinowitz, A. J. Tuzzolino, L. V. Ksanfomality and R. Z. Sagdeev (1987), The dust coma of comet 1P/Halley: measurements on the Vega-1 and Vega-2 spacecraft, *Astron. Astrophys.* **187**, 742-752.

Soderblom, L. A., *et al.* (2004), Imaging Borrelly, *Icarus* **167**, 4-15.

Thomas, N. and H. U. Keller (1987), Fine dust structures in the emission of comet P/Halley observed by the Halley Multicolour Camera on board Giotto, *Astron. Astrophys.* **187**, 843-846.

Tsou, P., D. E. Brownlee, S. A. Sandford, F. Horz and M. E. Zolensky (2003), Wild 2 and interstellar sample collection and Earth return, *J. Geophys. Res*., **108**, E10, SRD-3 1-21.

Tsou, P. *et al.* (2004), STARDUST encounters comet 81P/Wild 2, *J. Geophys. Res.,* submitted.

Tuzzolino, A. J. *et al*. (2003), Dust Flux Monitor Instrument for the Stardust mission to comet Wild 2, *J. Geophys. Res*., **108**(E10), SRD-5 1-24.

Tuzzolino, A. J., T. E. Economou, B. C. Clark, P. Tsou, D. E. Brownlee, J. A. M. McDonnell, S. F. Green, N. McBride and M. C. T. Colwell (2004), Dust measurements in the coma of comet 81P/Wild 2 by the Dust Flux Monitor Instrument, *Science*, **304**, 1776-1780.

Vaisberg, O. L., V. Smirnov, A. Omelchenko, L. Gorn and M. Iovlev (1987), Spatial and mass distributions of low-mass dust particles ($m < 10^{-10}$ g) in comet P/Halley's coma, *Astron. Astrophys.* **187**, 753-760.

Figure Captions

Figure 1. View of the Stardust spacecraft along the relative velocity vector during 81P/Wild 2 flyby, indicating the relative areas of active and inactive surfaces exposed to cometary dust impacts. The sensitive areas of the DFMI sensors are shaded. The acoustic sensor located on the rear shield (A2), is directly behind the A1 sensor.

Figure 2. Schematic of the DFMI acoustic sensor output for counts resulting in N_1=3 and N_2=3 (see text for details).

Figure 3. Acoustic sensor peak output voltage V_p as a function of impactor mass at 6.1 km s^{-1}, and 4cm from the sensor. The data are unamplified signals (20x amplification is performed in the flight electronics). a) Data for all particles with well determined signals and momentum. The non-penetrating glass impact apparently above the penetration threshold was in fact the combined signal from several small non-penetrating particles. b) Best fit obtained for non-penetrating particles with signals in the regime where the detector output is linear.

Figure 4. a) Relative sensitivity of the acoustic sensor output as a function of position on the Stardust front shield. b) Response as a function of distance *r* from the sensor. The large squares and circles are for data parallel and perpendicular to the straight edge of the hemispherical shield section (and passing through the sensor location).

Figure 5. a) The variation of effective area of the acoustic detector on the front shield as a function of cumulative mass index of the impacting particles. b) The fraction of detected particles which are larger than the defined mass threshold of 3 x 10^{-11} kg (see text for details).

Figure 6. The main features of the 81P/Wild 2 encounter data from DFMI. The upper section shows all the encounter data at 1 second resolution for the most sensitive channels of the PVDF and acoustic sensors. The PVDF data are shown on a logarithmic scale. The acoustic data (underneath) are on a linear scale. The middle section shows, in more detail, a 200 second period, centered on closest approach. The lower section shows the data at the highest possible resolution (0.1 s for PVDF and 1 sec for acoustic sensors) for the period from closet approach to +20 s.

Figure 7. The cumulative mass distribution along the trajectory of Stardust for the entire Wild 2 encounter. Open symbols with downward arrows indicate upper limits that correspond to one impact. The solid line is the best fit mass distribution ($\alpha = 0.85$) for $m < 10^{-9}$ kg. On the upper axis the particle size is indicated assuming a density of 500 kg m^{-3}. This is for illustrative purposes only as the true density is unknown and may vary with mass.

Figure 8. a) The cumulative mass distribution in the inner coma of Wild 2 (particles detected within 600 s of closest approach). Open symbols with arrows indicate upper limits corresponding to one impact. The solid line is the best fit mass distribution ($\alpha = 0.75$) for $m < 10^{-9}$ kg. At larger masses an excess of larger particles (dashed line) similar to that seen in Halley, better fits the limited data available than an extrapolation of the distribution at small sizes (dotted line). b) The

Wild 2 mass distribution is compared with the mass distributions for comets Halley [*McDonnell et al.,* 1987] and Grigg-Skjellerup [*McDonnell et al.,* 1993].

Figure 9. Stardust DFMI data rebinned at the same spatial resolution as the Giotto DIDSY data that were obtained at 1P/Halley [*McDonnell et al*., 1987]. It is clear that fine detail, if it existed on the same spatial scales as at 81P/Wild 2, would not have been seen at Halley, and large variations would not have been apparent in the acoustic data.

Figure 10. Cumulative mass distributions for sample periods of DFMI data. Open symbols with arrows indicate upper limits corresponding to one impact. a) For the period between –33 s and –25 s. The solid line is the best fit mass distribution ($\alpha = 0.75$) for $m < 10^{-9}$ kg. b) For the period between +2 s and +4 s. The solid line is the best fit mass distribution ($\alpha = 0.75$) for $m < 10^{-11}$ kg. c) For the entire period up to –33 s. The solid line is the best fit mass distribution ($\alpha = 0.33$) for $m < 10^{-9}$ kg. d) For the period between –12 s and +2 s. The dashed line has a mass distribution index, $\alpha = 0.3$.

Figure 11. Cumulative mass distribution for particles detected after +600 s (i.e. during the second region of high activity at >3500 km from the nucleus) where the best fit mass distribution ($\alpha = 1.13$) indicates a dominance of small particles. Open symbols with arrows indicate upper limits corresponding to one impact.

Table 1. Particle fluences measured by DFMI at 81P/Wild 2. The second high-activity period occurs after +600 s.

			Total		t < +600 s		t > +600s	
Channel	Mass threshold (kg)	A_{eff} (m^2)	n*	Fluence (m^{-2})	n*	Fluence (m^{-2})	n*	Fluence (m^{-2})
m1	9.8×10^{-15}	0.002	8662	$(4.33\pm0.05)\times10^6$	1790	$(9.0\pm0.2)\times10^5$	6872	$(3.44\pm0.04)\times10^6$
m2	1.2×10^{-13}	0.002	93	$(4.65\pm0.5)\times10^4$	81	$(4.05\pm0.5)\times10^4$	12	6000±1700
m3	4.3×10^{-12}	0.002	26	$(1.30\pm0.26)\times10^4$	21	$(1.05\pm0.23)\times10^4$	5	2500±1100
m4	6.3×10^{-10}	0.002	0	< 500	0	< 500	0	< 500
M1	8.5×10^{-11}	0.02	21	$(1.05\pm0.23)\times10^3$	21	$(1.05\pm0.23)\times10^3$	0	< 50
M2	1.7×10^{-9}	0.02	1	50±50	1	50±50	0	< 50
M3	1.4×10^{-8}	0.02	0	< 50	0	< 50	0	< 50
M4	1.5×10^{-7}	0.02	0	< 50	0	< 50	0	< 50
AC1	3×10^{-8}	variable†	133	$(1.12\pm0.25)\times10^3$	130	$(1.08\pm0.25)\times10^3$	3	39±23
AC2	3×10^{-7}	variable†	41	34±5	40	330±50	1	13±13
AC3	2×10^{-7}	$0.3\ ^{+0.4}/_{-0.2}$	7	$23\ ^{+70}/_{-14}$	7	$23\ ^{+70}/_{-14}$	0	< 10
AC4	2×10^{-6}	$0.3\ ^{+0.4}/_{-0.2}$	1	$3\ ^{+10}/_{-3}$	1	$3\ ^{+10}/_{-3}$	0	< 10

*The cumulative number of impacts detected above the mass threshold for the given sensor.

†The acoustic sensor effective area depends on the cumulative mass distribution itself (see text and figure 5 for details.

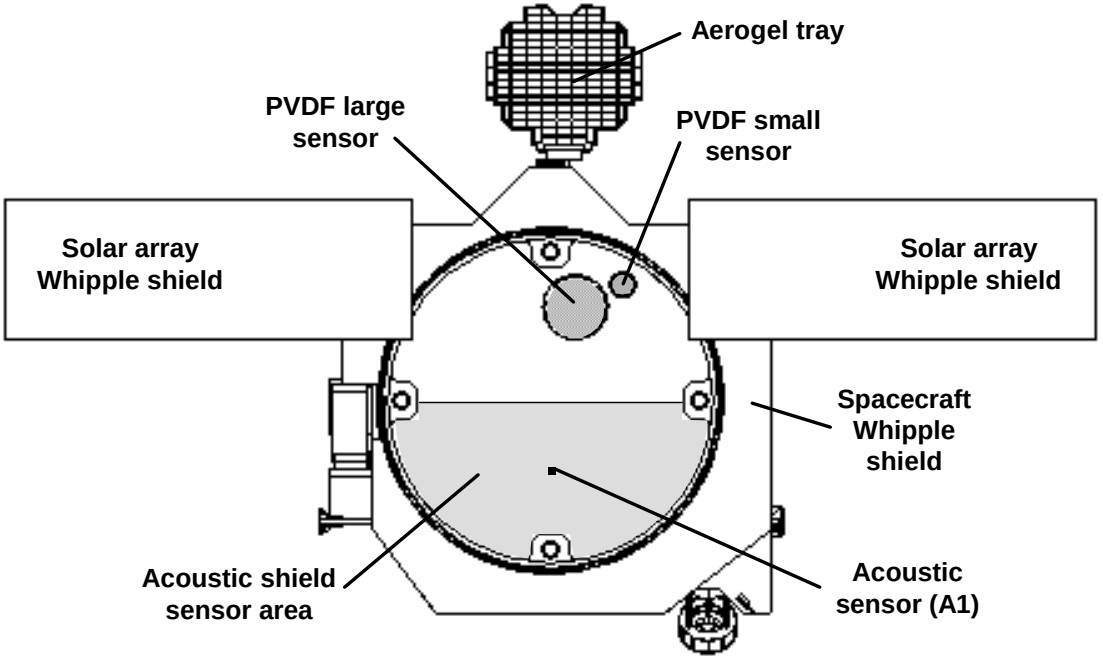
Aerogel tray
PVDF large sensor
PVDF small sensor
Solar array Whipple shield
Solar array Whipple shield
Spacecraft Whipple shield
Acoustic shield sensor area
Acoustic sensor (A1)

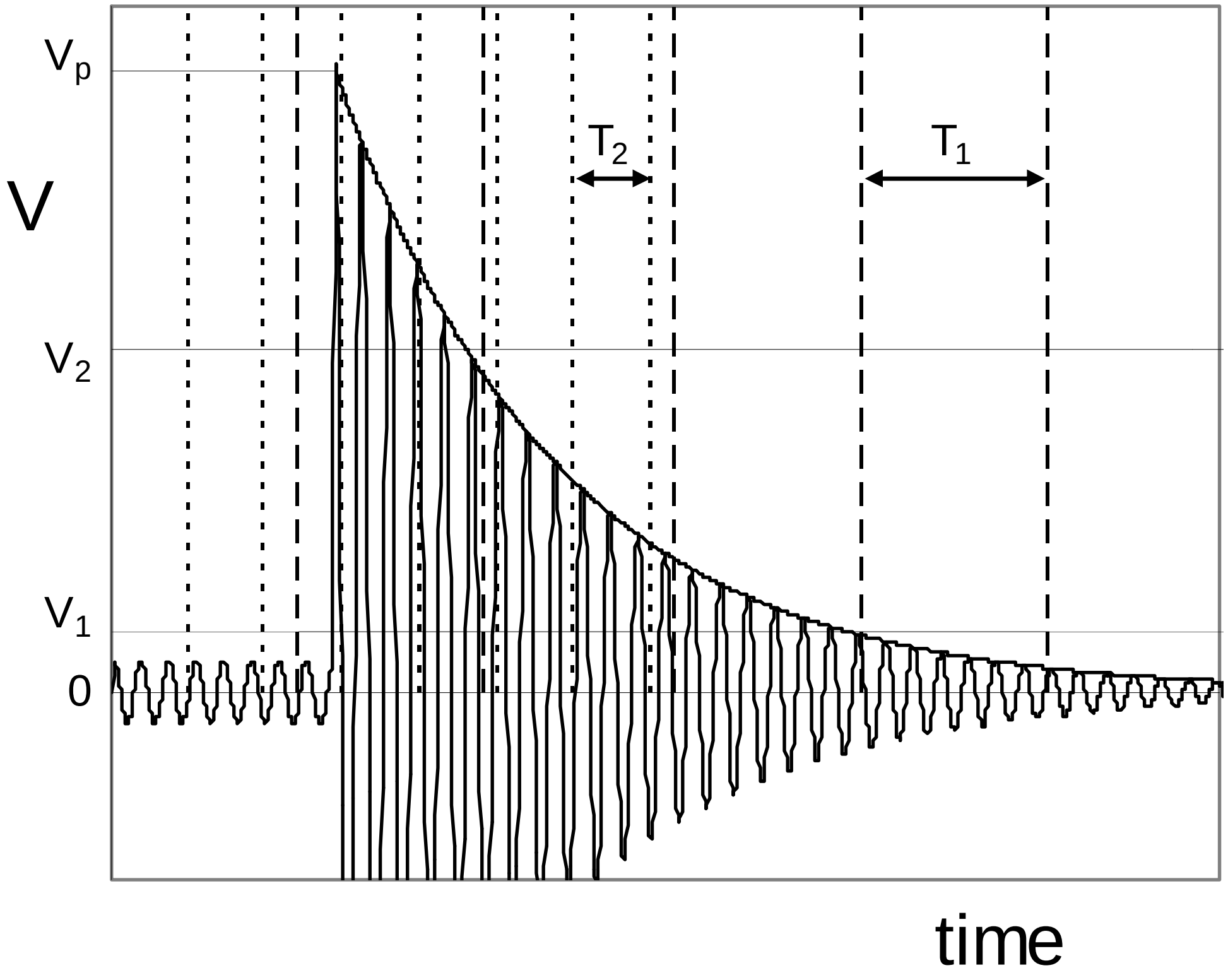
V_p
V
V_2
V_1
0
T_2
T_1
time

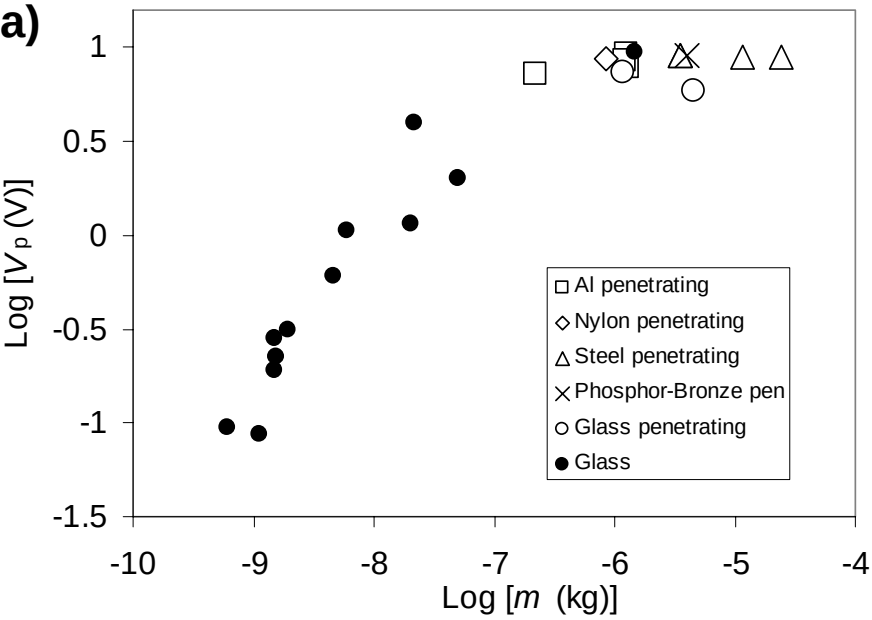
a)
1
0.5
0
-0.5
-1
-1.5
Log [V_p (V)]
-10
-9
-8
-7
-6
-5
-4
Log [m (kg)]
Al penetrating
Nylon penetrating
Steel penetrating
Phosphor-Bronze pen
Glass penetrating
Glass

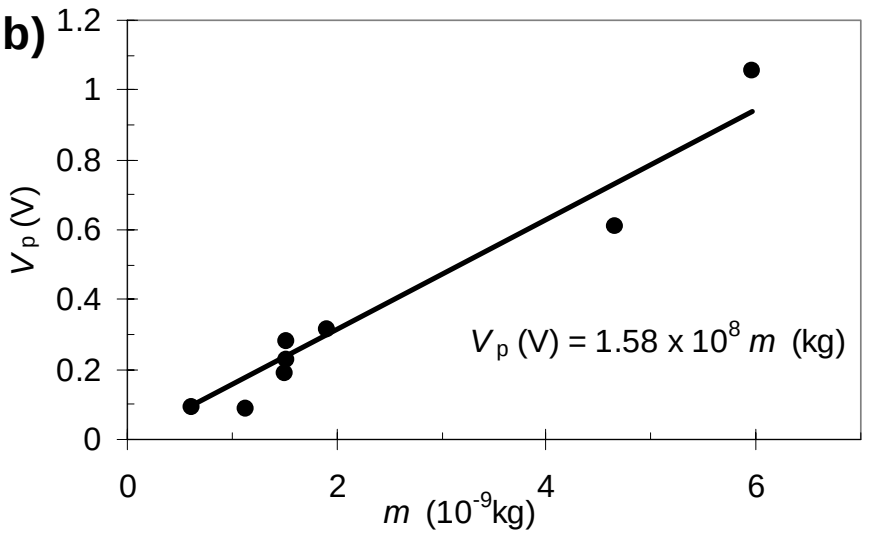
b)
1.2
1
0.8
0.6
0.4
0.2
0
V_p (V)
V_p (V) = 1.58 x 10^8 m (kg)
0
2
4
6
m (10^{-9}kg)

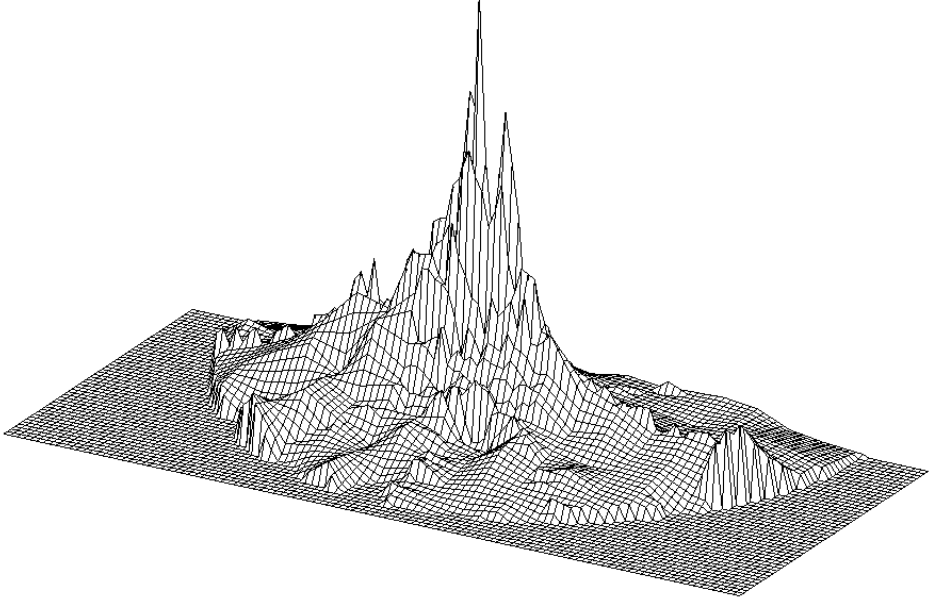

a)

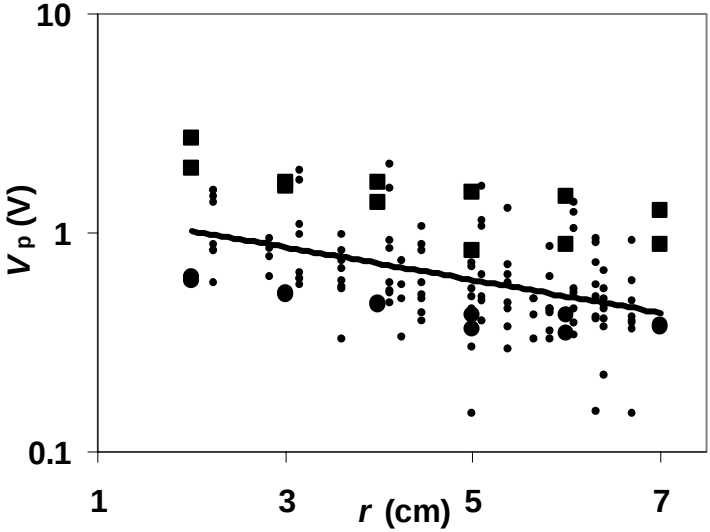

b)

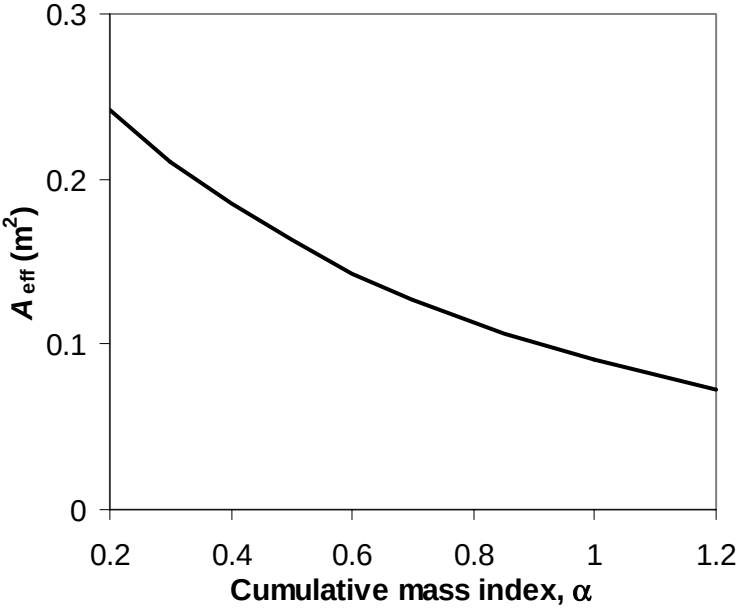
0.3
0.2
0.1
0
A_{eff} (m^2)
0.2
0.4
0.6
0.8
1
1.2
Cumulative mass index, α

a)

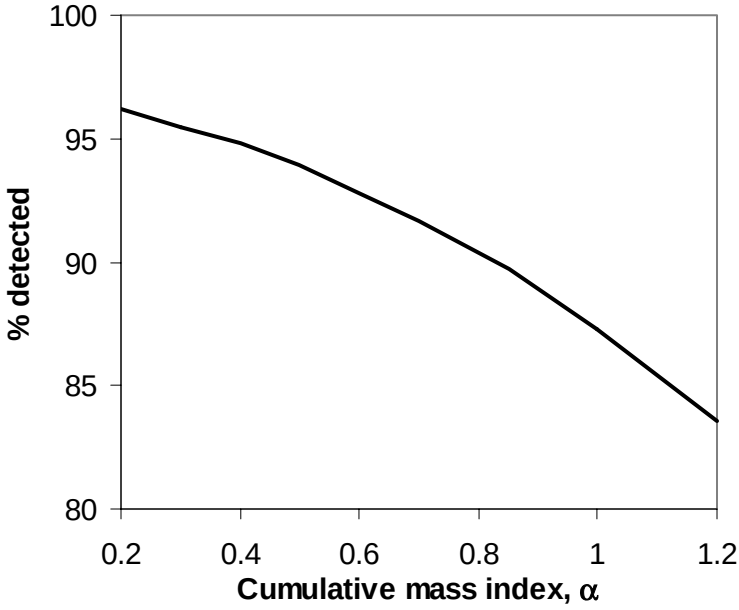
100
95
90
85
80
% detected
0.2
0.4
0.6
0.8
1
1.2
Cumulative mass index, α

b)

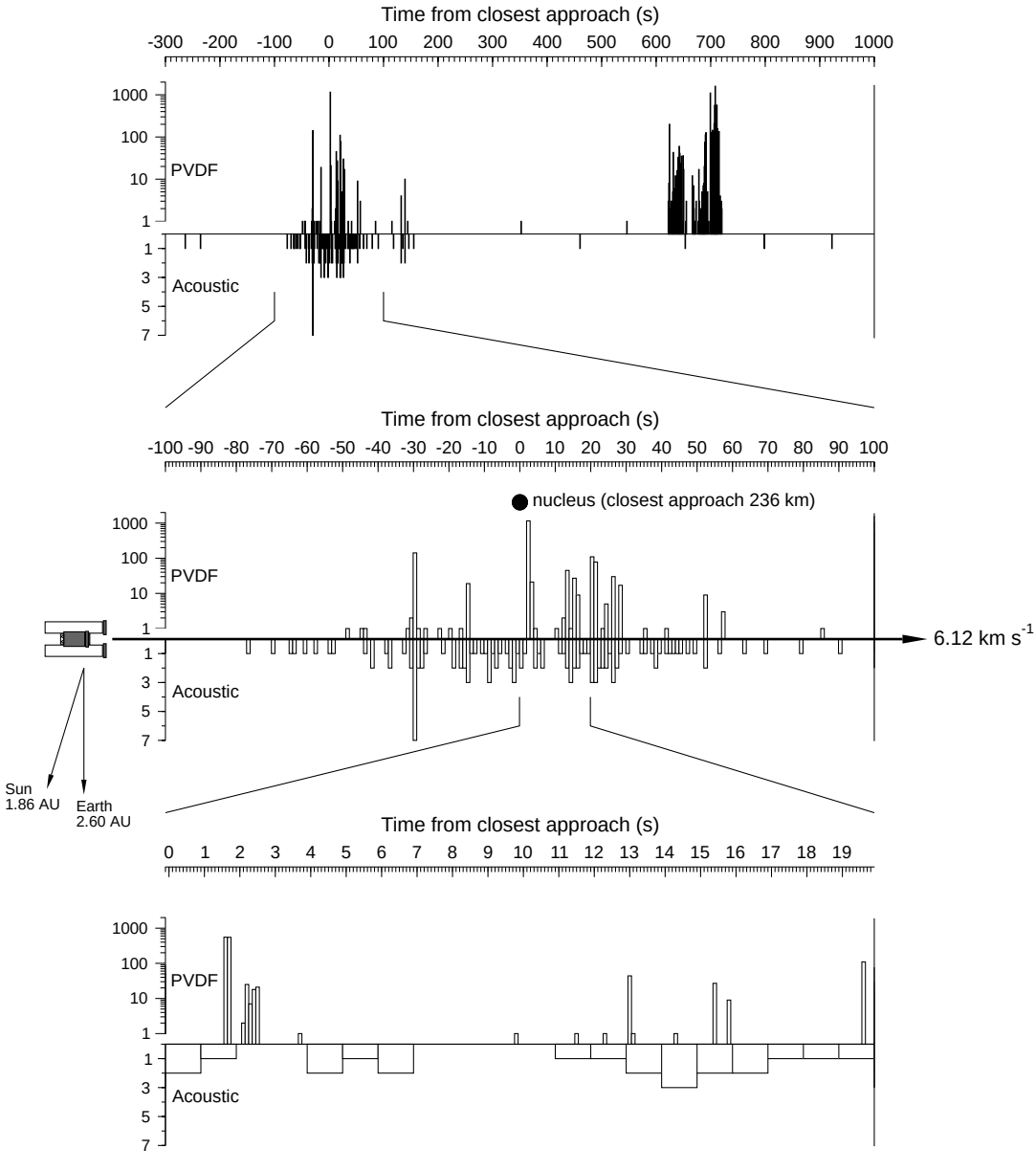
Time from closest approach (s)
-300 -200 -100 0 100 200 300 400 500 600 700 800 900 1000
1000
100
10
1
PVDF
1
3
5
7
Acoustic
Time from closest approach (s)
-100 -90 -80 -70 -60 -50 -40 -30 -20 -10 0 10 20 30 40 50 60 70 80 90 100
nucleus (closest approach 236 km)
1000
100
10
1
PVDF
1
3
5
7
Acoustic
6.12 km s-1
Sun
1.86 AU
Earth
2.60 AU
Time from closest approach (s)
0 1 2 3 4 5 6 7 8 9 10 11 12 13 14 15 16 17 18 19
1000
100
10
1
PVDF
1
3
5
7
Acoustic

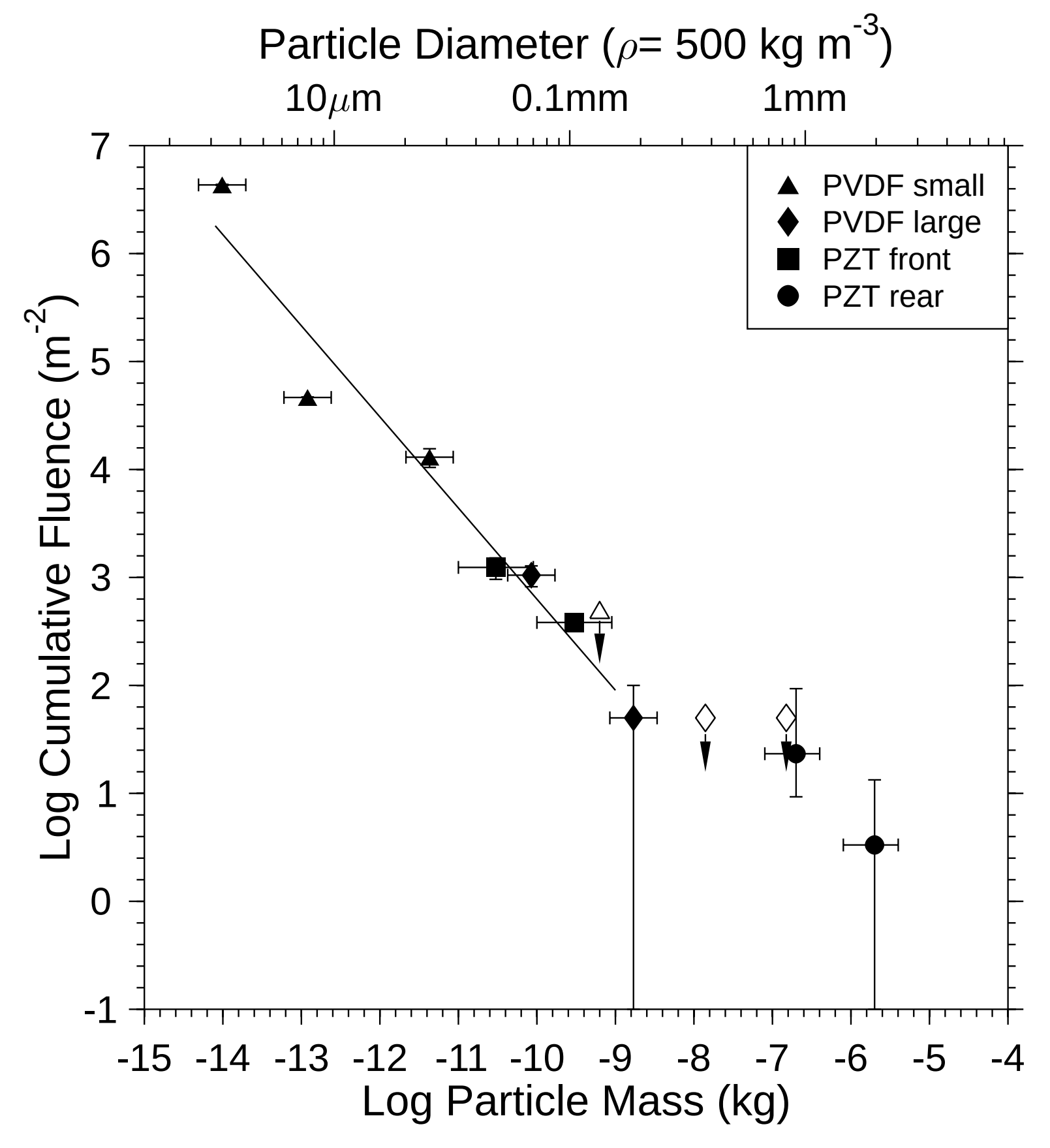
Particle Diameter (ρ= 500 kg m^{-3})
10μm
0.1mm
1mm
PVDF small
PVDF large
PZT front
PZT rear
Log Cumulative Fluence (m^{-2})
Log Particle Mass (kg)
7
6
5
4
3
2
1
0
-1
-15
-14
-13
-12
-11
-10
-9
-8
-7
-6
-5
-4

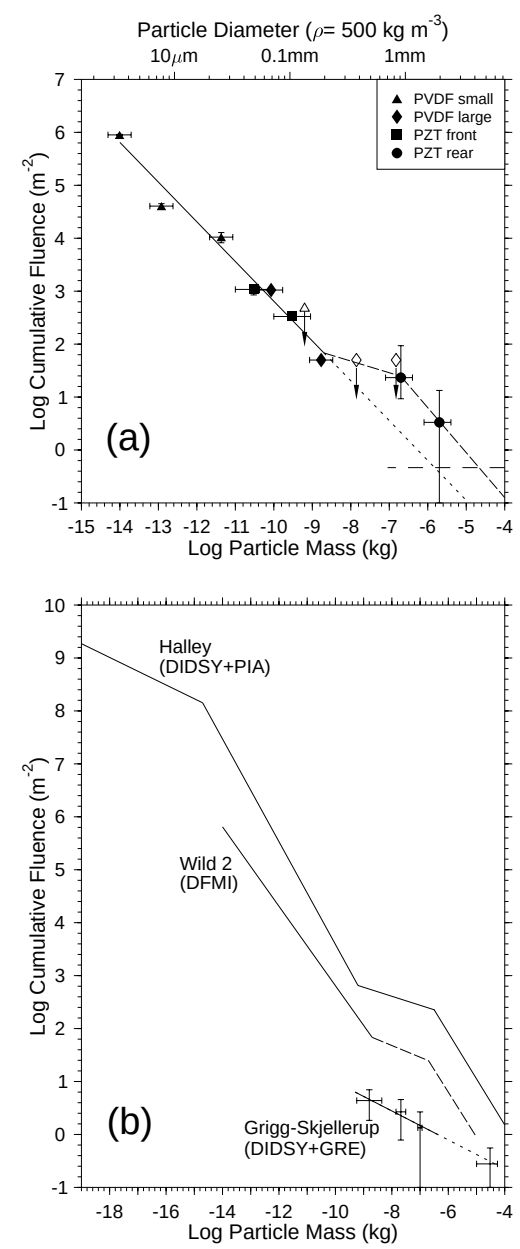
Particle Diameter (ρ= 500 kg m^{-3})
10μm
0.1mm
1mm
PVDF small
PVDF large
PZT front
PZT rear
Log Cumulative Fluence (m^{-2})
(a)
Log Particle Mass (kg)
Halley
(DIDSY+PIA)
Wild 2
(DFMI)
Grigg-Skjellerup
(DIDSY+GRE)
(b)
Log Cumulative Fluence (m^{-2})
Log Particle Mass (kg)

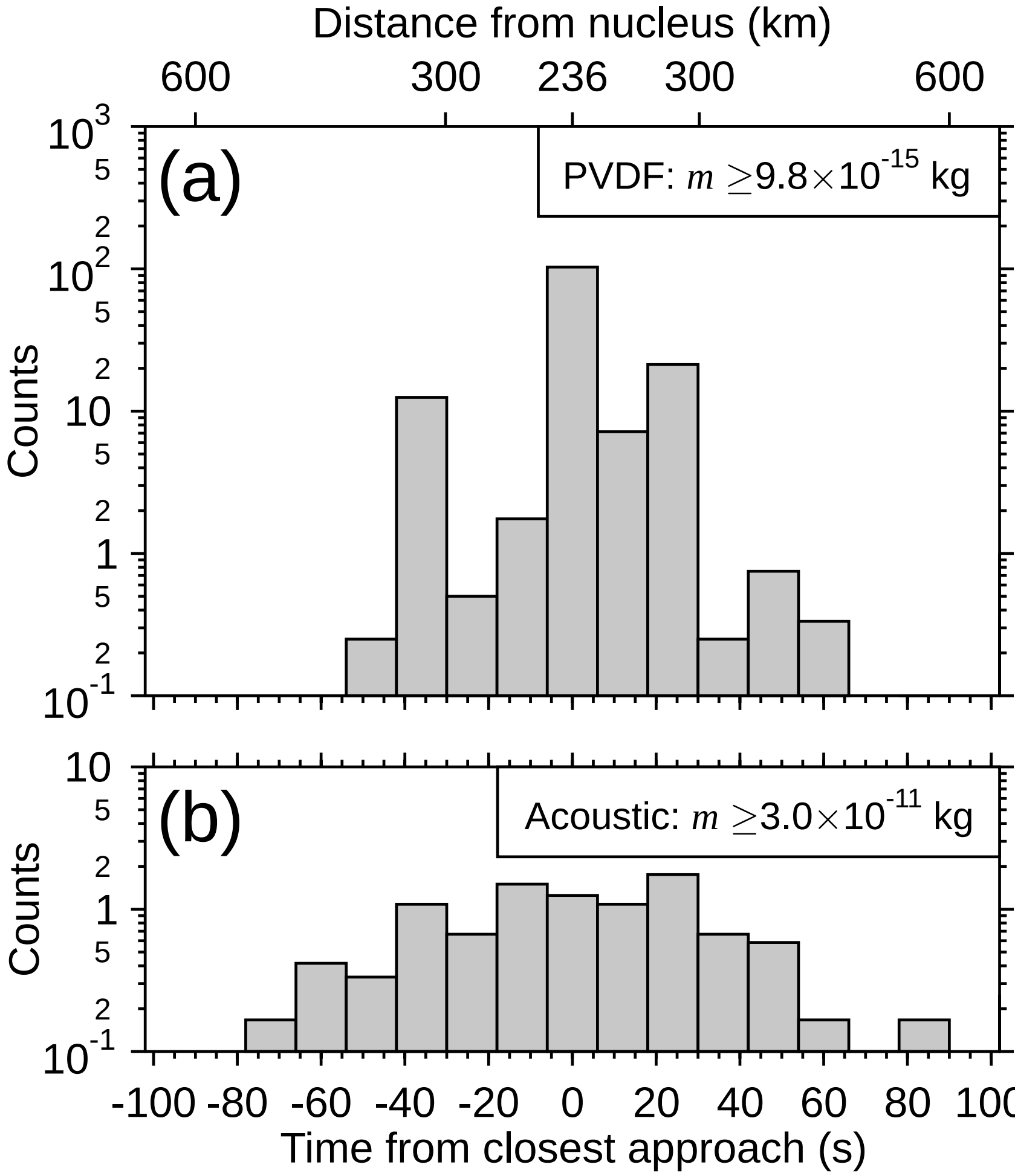
Distance from nucleus (km)
600
300
236
300
600
(a)
PVDF: $m \geq 9.8 \times 10^{-15}$ kg
Counts
10^3
5
2
10^2
5
2
10
5
2
1
5
2
10^{-1}
(b)
Acoustic: $m \geq 3.0 \times 10^{-11}$ kg
Counts
10
5
2
1
5
2
10^{-1}
-100
-80
-60
-40
-20
0
20
40
60
80
100
Time from closest approach (s)

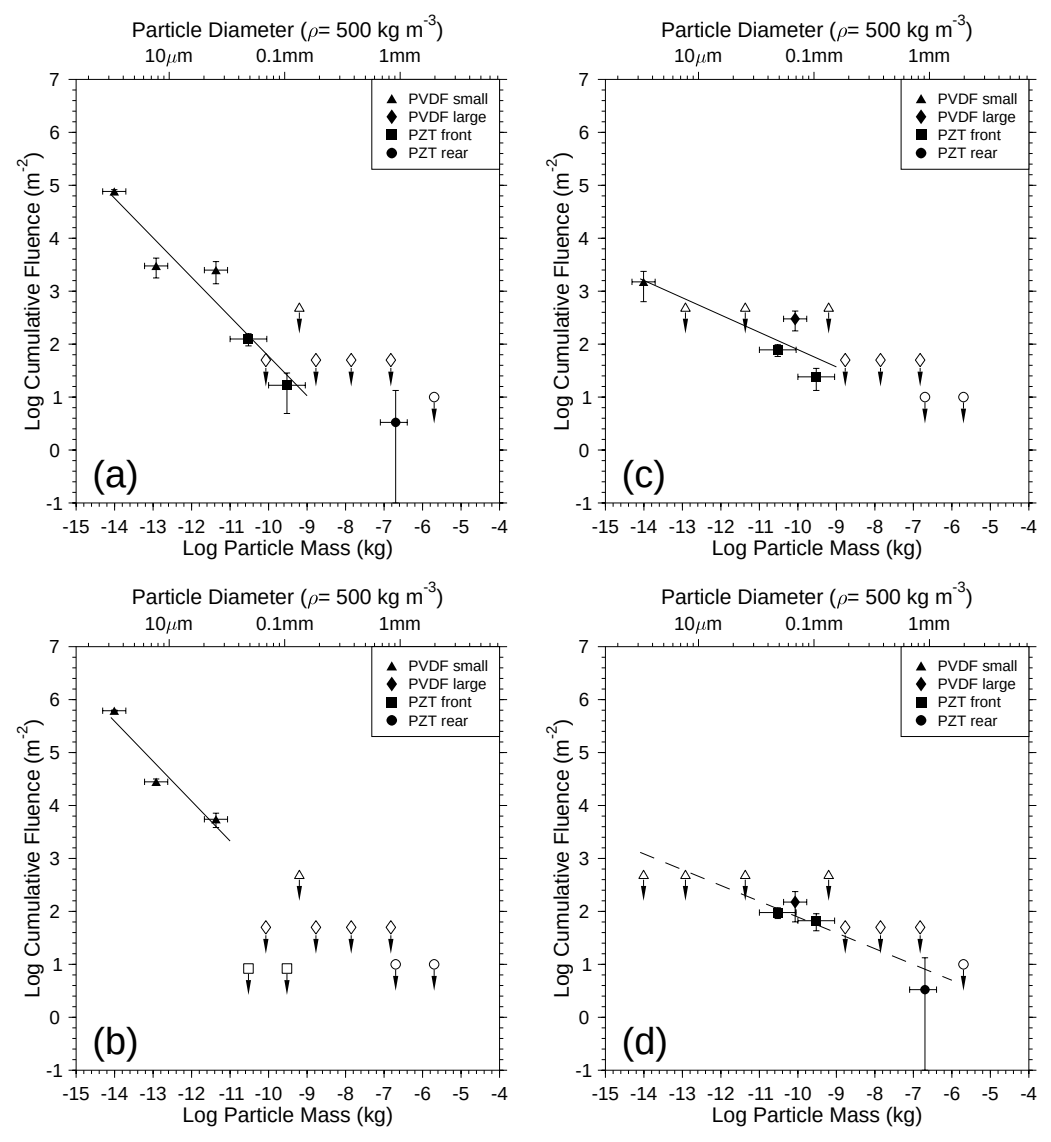
Particle Diameter (ρ= 500 kg m^{-3})
10μm
0.1mm
1mm
PVDF small
PVDF large
PZT front
PZT rear
Log Cumulative Fluence (m^{-2})
Log Particle Mass (kg)
(a)
(b)
(c)
(d)

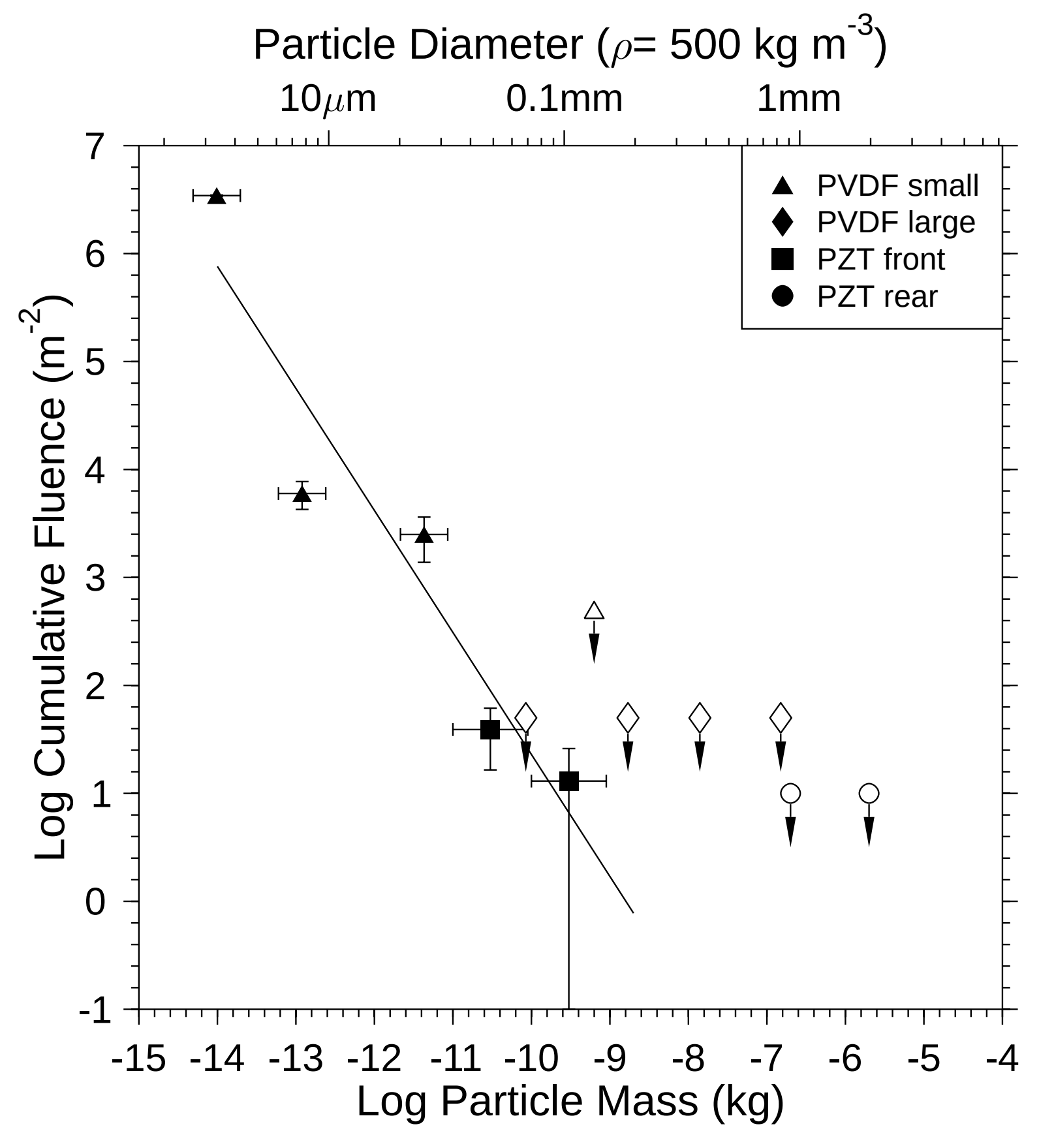
Particle Diameter (ρ= 500 kg m^{-3})
10μm
0.1mm
1mm
PVDF small
PVDF large
PZT front
PZT rear
Log Cumulative Fluence (m^{-2})
Log Particle Mass (kg)
7
6
5
4
3
2
1
0
-1
-15
-14
-13
-12
-11
-10
-9
-8
-7
-6
-5
-4